AIAA JOURNAL
Vol. 42, No. 11, November 2004

Laminar Incompressible Flow past Parabolic Bodies at Angles of Attack

E. Erturk*
Gebze Institute of Technology, 41400 Gebze–Kocaeli, Turkey
O. M. Haddad†
Jordan University of Science and Technology, 22110 Irbid, Jordan
and
T. C. Corke‡
University of Notre Dame, Notre Dame, Indiana 46556

Numerical solutions of a two-dimensional steady laminar incompressible flow over semi-infinite parabolic bodies at angles of attack are obtained. All solutions are found by using a modified numerical approach to solve the time-dependent Navier–Stokes equations. The governing equations are written for the stream function and vorticity variables and are solved on a nonuniform body-fitted parabolic grid. A check of our solutions to those that exist in the literature at zero angle of attack showed excellent agreement. In addition, at zero angle of attack far from the leading edge, an expected correspondence to Blasius flow was found. At positive angles of attack, the body became aerodynamically loaded with lower pressures on its upper surface. At large enough angles of attack, the flow separated on the upper surface. In all of the cases examined, the flow separation was followed by a reattachment that defined a separation zone. An almost linear increase in the streamwise extent of the separation zone occurred with increasing angle of attack. The separation location and extent of the separation zone was a function of the nose Reynolds number. The results indicated that the shape factor could be used to provide a criterion for separation and reattachment in these cases. The characteristics of the separation zone for this geometry should prove to be an excellent basic flow to document the effect of leading-edge flow separation on acoustic receptivity of boundary-layer instabilities.

Nomenclature

C_f	=	skin friction coefficient
g	=	modified vorticity
H	=	shape factor
i	=	numerical index in streamwise direction
$i$buf	=	index i at the beginning of the buffer zone
$i$max	=	numerical index of the last grid point in streamwise direction
j	=	numerical index in the wall normal direction
P	=	nondimensional pressure
p	=	pressure
R	=	nose radius of curvature
Re	=	Reynolds number (or nondimensional nose radius of curvature)
r	=	radius of curvature
s	=	weighting factor
t	=	time
U_∞	=	freestream velocity
(u, v)	=	velocity components in the (x, y) directions, respectively
(x, y)	=	Cartesian coordinates
α	=	angle of attack
β	=	stretching factor
Δ	=	difference
δ_1	=	displacement thickness
δ_2	=	momentum thickness
ν	=	kinematic viscosity
(ξ, η)	=	parabolic coordinates
ρ	=	density
τ	=	shear stress
ψ	=	stream function
ω	=	vorticity

Subscripts

r	=	reattachment
s	=	separation
w	=	wall

Superscripts

n	=	iteration number
$*$	=	dimensional quantity

I. Introduction

THE importance of the flow over parabolic bodies comes from that aerodynamic bodies designed for subsonic flow generally have finite thickness distributions with parabolic leading edges.[1] In addition, because the flow on parabolic bodies proceeds without separation from stagnation point flow at the nose to Blasius flow farther downstream, the flow over parabolic bodies represents the flow over flat plates more closely, with the effect of blunt leading edge being implicitly considered if the leading-edge region is not excluded from the solution domain.

Van Dyke[2] presented one of the earliest analysis in which the classical laminar boundary layer on a parabolic cylinder was calculated using Blasius series. He considered that there is no singularity at the nose of the parabolic body, as in the case of the semi-infinite flat plate. Davis[3] studied the laminar flow past a semi-infinite flat plate using parabolic coordinates. In his study, he used a series truncation

Received 22 July 2003; revision received 20 January 2004; accepted for publication 11 May 2004.

*Assistant Professor, Energy Systems Engineering Department, College of Engineering; ercanerturk@gyte.edu.tr.
†Associate Professor, Department of Mechanical Engineering, P.O. Box 3030; haddad@just.edu.jo.
‡Clark Chair Professor, Department of Aerospace and Mechanical Engineering; tcorke@nd.edu. Associate Fellow AIAA.

method in which the stream function was locally expanded in a power series.

When parabolic coordinates are used, the flow over parabolic body is the natural extension of the flow over a flat plate. Dennis and Walsh[4] obtained a numerical solution for the steady symmetric viscous flow past a parabolic cylinder in a uniform stream. They obtained the solution of the partial differential equations for stream function and vorticity using two-dimensional finite difference approximations. Their study covered the range of Reynolds number (based on the nose radius of the cylinder) from 0.25 to ∞. Davis[5] obtained numerical solutions of the Navier–Stokes equations for laminar symmetric incompressible flow over an infinitely long parabola. Solutions were found by using an alternating direction implicit method. Davis paid careful attention on extracting the singularities from the problem in the limit as Reynolds number goes to zero, that is, infinitesimal flat plate solution. In a more recent study, Gatski[6] have numerically calculated the two-dimensional laminar incompressible flow over a parabolic cylinder at zero angle of attack. For this purpose, the finite difference method was used to solve the Navier–Stokes equations in vorticity–velocity variables. In his study, Gatski was interested in cylinders of very small radii, smaller than the Tollmein–Schlichting (T–S) instability wavelength of the boundary-layer flow.

In recent studies by the authors, the acoustic receptivity of laminar incompressible boundary layers over parabolic bodies at zero incidence have been investigated numerically. Haddad and Corke[7] focused on the effect of the nose radius of curvature of the parabolic body, that is, bluntness, on the receptivity process. Numerical solutions were obtained for the Navier–Stokes equations in stream function and vorticity variables to determine the receptivity coefficient at the leading edge of the body. Erturk[8] and Erturk and Corke[9] extended this study and introduced acoustic waves at incidence angles with respect to the parabolic body axis to document its effect on the leading-edge receptivity coefficient. Wanderley and Corke[10] applied this approach to an elliptic leading edge to investigate the apparent frequency selection mechanism observed in experiments of Saric and White.[11] Haddad et al.[12] included the energy equation in their analysis and carried out the first study to investigate the steady laminar forced convection flow over parabolic bodies. This work documented the effect of leading-edge bluntness on the rate of heat transfer. Haddad et al.[13] included the effect of a porous medium surrounding the parabolic body on the flow and heat transfer characteristics. This involved the solution of the full Navier–Stokes equations, combined with the Brinkman–Forchheimer-extended Darcy model, and energy equations in parabolic coordinates.

All of the previous literature on the flow over parabolic bodies has been at zero angle of attack. Because all practical aerodynamic bodies are aerodynamically loaded, there is a natural interest in the effect this has on the acoustic receptivity leading to boundary-layer instabilities. The first step toward this is to calculate accurately the mean flow distribution. This is the emphasis of this paper. A study on the receptivity of this flow to acoustic disturbance is intended to follow from this.

II. Mathematical Formulation of the Physical Problem

Figure 1 shows a schematic diagram of the parabolic body set at mean angle of attack with respect to a uniform flow. The equation of the surface of the parabolic body is given by

$$x(y) = (1/2R)(y^2 - R^2) \tag{1}$$

where x and y are the Cartesian coordinates. Based on Eq. (1), it can be shown that R is equal to the nose radius of curvature of the parabola.

A. Governing Equations

In this study, the full Navier–Stokes (N–S) equations are considered. For a two-dimensional steady laminar incompressible flow, the N–S equations in stream function ψ and vorticity ω variables in the Cartesian coordinates are given in the form

$$\frac{\partial^2 \psi^*}{\partial x^{*2}} + \frac{\partial^2 \psi^*}{\partial y^{*2}} = -\omega^* \tag{2}$$

$$\frac{\partial \psi^*}{\partial y^*}\frac{\partial \omega^*}{\partial x^*} - \frac{\partial \psi^*}{\partial x^*}\frac{\partial \omega^*}{\partial y^*} = \nu\left(\frac{\partial^2 \omega^*}{\partial x^{*2}} + \frac{\partial^2 \omega^*}{\partial y^{*2}}\right) \tag{3}$$

where an asterisk denotes dimensional variable. To nondimensionalize the preceding equations, the following group of dimensionless variables is introduced:

$$x = x^*/(\nu/U_\infty), \qquad y = y^*/(\nu/U_\infty)$$

$$\omega = \omega^*\Big/\left(U_\infty^2\Big/\nu\right), \qquad \psi = \psi^*/\nu \tag{4}$$

In addition, the geometry of the body suggests that the problem be formulated in terms of parabolic coordinates. The dimensionless parabolic coordinates (ξ, η) are related to the dimensionless Cartesian coordinates (x, y) by

$$x + iy = (\xi + i\eta)^2/2 \tag{5}$$

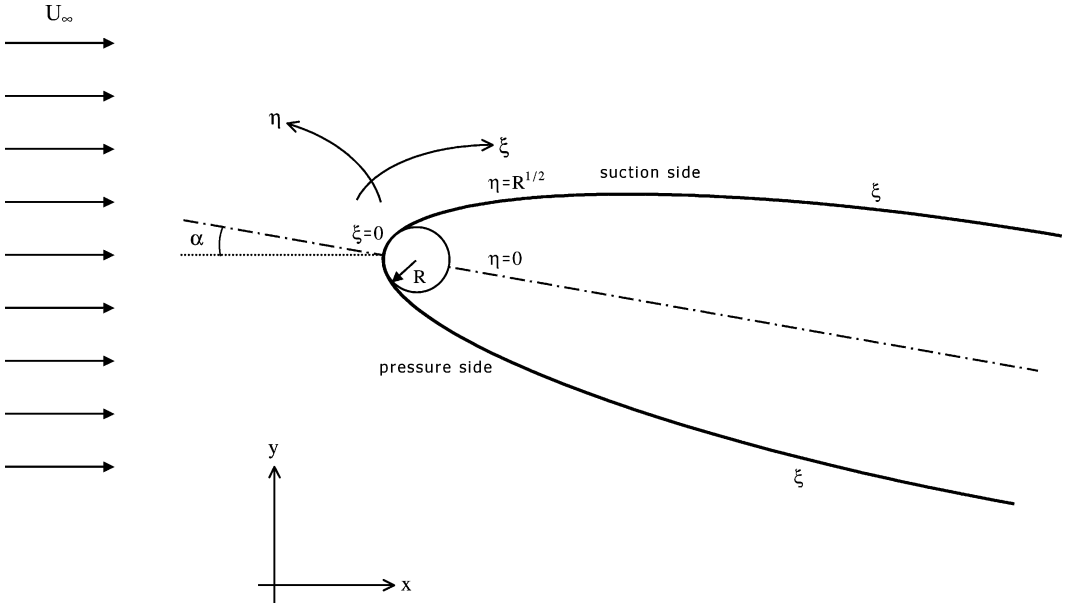

Fig. 1 Schematic diagram of parabolic body at angle of attack in uniform stream used to define the coordinate system for computational analysis.

or

$$x = (\xi^2 - \eta^2)/2, \qquad y = \xi\eta \tag{6}$$

where $i = \sqrt{-1}$.

Based on Eqs. (4) and (6), the governing equations (2) and (3) can be nondimensionalized and rewritten in parabolic coordinates as

$$\frac{\partial^2\psi}{\partial\xi^2} + \frac{\partial^2\psi}{\partial\eta^2} = -(\xi^2 + \eta^2)\omega \tag{7}$$

$$\frac{\partial^2\omega}{\partial\xi^2} + \frac{\partial^2\omega}{\partial\eta^2} + \frac{\partial\psi}{\partial\xi}\frac{\partial\omega}{\partial\eta} - \frac{\partial\psi}{\partial\eta}\frac{\partial\omega}{\partial\xi} = 0 \tag{8}$$

In a previous work, the authors have adopted the transformation introduced by Davis[5] to remove the singularity at the leading edge in the limiting case when $R = 0$, that is, infinitesimally thin flat plate. Because the present study is not concerned with zero thickness bodies, the authors decided not to consider Davis[5] transformations in the present study but to solve the preceding equations directly for ψ and ω for cases where $R > 0$.

B. Boundary Conditions

First, note that based on Eqs. (1) and (6), the body surface is located at $\eta_w = Re^{1/2}$. If R is nondimensionalized using the length scale introduced in Eq. (4), the dimensional nose radius of curvature, R, becomes Reynolds number Re based on the nose radius of curvature. Therefore, for fixed value of ν and U_∞, Reynolds number Re is a measure of the thickness of the parabolic body, that is, bluntness.

At the wall, the no-slip, no-penetration conditions are satisfied by

$$\psi\left(\xi, Re^{\frac{1}{2}}\right) = \text{const} = 0, \qquad \psi_\eta\left(\xi, Re^{\frac{1}{2}}\right) = 0 \tag{9}$$

Also, to generate a condition on the vorticity at the wall, the stream function equation (7) is applied at the wall where $\psi_\xi = \psi_{\xi\xi} = \psi_\eta = 0$, which yields

$$\omega\left(\xi, Re^{\frac{1}{2}}\right) = \left[-1\Big/\left(\xi^2 + \eta_w^2\right)\right]\psi_{\eta\eta} \tag{10}$$

On the other hand, the magnitude of the freestream velocity is set equal to unity because the freestream velocity has been used as a reference velocity scale in Eq. (4), that is,

$$|U_\infty| = 1 \tag{11}$$

therefore, the velocity components of the freestream with nonzero angle of attack will be

$$u = \cos(\alpha), \qquad v = \sin(\alpha) \tag{12}$$

where u and v are the respective velocity components in x and y directions and α is the angle of attack. Recall that the stream function is defined as

$$\frac{\partial\psi}{\partial y} = u, \qquad \frac{\partial\psi}{\partial x} = -v \tag{13}$$

therefore, the value of the stream function in the freestream should be defined as

$$\psi_\infty = y\cos(\alpha) - x\sin(\alpha) \tag{14}$$

Hence, when parabolic coordinates are used, the freestream boundary condition for the stream function as $\eta \to \infty$ is

$$\frac{\partial\psi}{\partial\eta} \to \xi\cos(\alpha) + \eta\sin(\alpha) \tag{15}$$

and for the vorticity condition, away from the wall, the potential flow has zero vorticity. Therefore, as $\eta \to \infty$

$$\omega \to 0 \tag{16}$$

III. Grid Generation

The contour of the body surface is defined by the line $\eta_w = Re^{1/2}$. The freestream is also defined by the line $\eta = \eta_{\max}$. The freestream is set to be at a distance from the wall that is at least 10 times the estimated maximum Blasius boundary-layer thickness on a flat plate of the same axial length as the parabolic body and at $\alpha = 0$. Therefore, in the wall normal direction, η varies between the values

$$Re^{\frac{1}{2}} \le \eta \le Re^{\frac{1}{2}} + 35 \tag{17}$$

On the surface of the body, the leading edge is located at $\xi = 0$. The outflow boundaries on the lower and upper sides of the body are located at $\xi = -\xi_{\max}$ and $\xi = +\xi_{\max}$. The outflow boundary is set far away from the leading edge at $x_{\max} = 3.5 \times 10^5$. Therefore, the last grid point in the streamwise direction [based on Eq. (6) and that $\eta_w = Re^{1/2}$] is located at $\xi_{\max} = (2x_{\max} + Re)^{1/2}$, that is, $\xi_{\max} \cong 837$.

To capture the physical phenomenon more accurately, more grid points were located near the wall in the η direction and near the leading edge in the ξ direction. This was done using Robert's stretching transformation of the original uniform grid (see Ref. 14). The transformation used is given by

$$y = h\frac{(\beta+1) - (\beta-1)[(\beta+1)/(\beta-1)]^{1-\bar{y}}}{[(\beta+1)/(\beta-1)]^{1-\bar{y}} + 1} \tag{18}$$

where $\bar{y}$ are the original uniformly spaced grid points, y are the stretched grid points, and β is the stretching parameter. In the present study $\beta = 1.25$ in the ξ direction, and $\beta = 1.005$ in the η direction because these values provided sufficiently accurate results.

IV. Numerical Method

This study is concerned with the steady-state solution governed by Eqs. (7) and (8). Equations (7) and (8) are elliptic and can be directly solved by many different numerical methods. Such approaches have been successfully used by several investigators, but they appear to be susceptible to instabilities.[14] For this reason, a pseudotransient approach is recommended and, thus, was used in this study to obtain steady-state solutions of the problem.

The construction of pseudotransient equations yields

$$\frac{\partial\psi}{\partial t} = \frac{\partial^2\psi}{\partial\xi^2} + \frac{\partial^2\psi}{\partial\eta^2} + (\xi^2 + \eta^2)\omega \tag{19}$$

$$\frac{\partial\omega}{\partial t} = \frac{\partial^2\omega}{\partial\xi^2} + \frac{\partial^2\omega}{\partial\eta^2} + \frac{\partial\psi}{\partial\xi}\frac{\partial\omega}{\partial\eta} - \frac{\partial\psi}{\partial\eta}\frac{\partial\omega}{\partial\xi} \tag{20}$$

Consequently, one now solves two parabolic equations. The equations may be solved sequentially or as a coupled system.

To solve Eqs. (19) and (20), a numerical method was developed. This is based on the approximate factorization principle, with some modifications. A brief description of the method is provided next.

The finite difference formulation used for Eqs. (19) and (20) is

$$\left(1 - \Delta t\frac{\partial^2}{\partial\xi^2} - \Delta t\frac{\partial^2}{\partial\eta^2}\right)\psi^{n+1} = \psi^n + \Delta t(\xi^2 + \eta^2)\omega^n \tag{21}$$

$$\left[1 - \Delta t\frac{\partial^2}{\partial\xi^2} - \Delta t\frac{\partial^2}{\partial\eta^2} - \Delta t\left(\frac{\partial\psi}{\partial\xi}\right)^n\frac{\partial}{\partial\eta} + \Delta t\left(\frac{\partial\psi}{\partial\eta}\right)^n\frac{\partial}{\partial\xi}\right]\omega^{n+1} = \omega^n \tag{22}$$

This is a fully implicit form and, thus, requires the solution of a large matrix that is computationally inefficient. Instead, we spatially factorize the equations such that

$$\left(1 - \Delta t\frac{\partial^2}{\partial\xi^2}\right)\left(1 - \Delta t\frac{\partial^2}{\partial\eta^2}\right)\psi^{n+1} = \psi^n + \Delta t(\xi^2 + \eta^2)\omega^n \tag{23}$$

$$\left[1-\Delta t\frac{\partial^2}{\partial\xi^2}+\Delta t\left(\frac{\partial\psi}{\partial\eta}\right)^n\frac{\partial}{\partial\xi}\right]\times\left[1-\Delta t\frac{\partial^2}{\partial\eta^2}-\Delta t\left(\frac{\partial\psi}{\partial\xi}\right)^n\frac{\partial}{\partial\eta}\right]\omega^{n+1}=\omega^n \tag{24}$$

The advantage of this process is that Eqs. (23) and (24) require the solution of tridiagonal systems that can be solved very efficiently using the Thomas algorithm.

When the two operators in Eqs. (23) and (24) are multiplied, it can be shown that approximate factorization introduces an additional term of $\mathcal{O}(\Delta t^2)$ in these equations. To overcome this problem, the numerical method was modified to cancel out the resulting $\mathcal{O}(\Delta t^2)$ terms due to the factorization. This is done by adding the same terms at a previous time step to the right-hand side (RHS) of Eqs. (23) and (24). This makes the final form of the factorized finite difference equations

$$\left(1-\Delta t\frac{\partial^2}{\partial\xi^2}\right)\left(1-\Delta t\frac{\partial^2}{\partial\eta^2}\right)\psi^{n+1}=\psi^n+\Delta t(\xi^2+\eta^2)\omega^n+\left(\Delta t\frac{\partial^2}{\partial\xi^2}\right)\left(\Delta t\frac{\partial^2}{\partial\eta^2}\right)\psi^n \tag{25}$$

$$\left[1-\Delta t\frac{\partial^2}{\partial\xi^2}+\Delta t\left(\frac{\partial\psi}{\partial\eta}\right)^n\frac{\partial}{\partial\xi}\right]\left[1-\Delta t\frac{\partial^2}{\partial\eta^2}-\Delta t\left(\frac{\partial\psi}{\partial\xi}\right)^n\frac{\partial}{\partial\eta}\right]\omega^{n+1}=\omega^n+\left[\Delta t\frac{\partial^2}{\partial\xi^2}-\Delta t\left(\frac{\partial\psi}{\partial\eta}\right)^n\frac{\partial}{\partial\xi}\right]\times\left[\Delta t\frac{\partial^2}{\partial\eta^2}+\Delta t\left(\frac{\partial\psi}{\partial\xi}\right)^n\frac{\partial}{\partial\eta}\right]\omega^n \tag{26}$$

Note that the added $\mathcal{O}(\Delta t^2)$ terms on the RHS are not artificial numerical diffusion terms. Such terms are often used to stabilize the numerical schemes so that convergence can be achieved. However, the added $\mathcal{O}(\Delta t^2)$ terms are not meant to stabilize the numerical scheme. Their purpose is to cancel out the terms introduced by factorization so that the equations have the correct physical representation at steady state. More details about the numerical method can be found by Erturk.[8,15] The method is very suitable for solving two-dimensional incompressible N–S problems. The power of the method was demonstrated in a previous study by Erturk and Corke.[9]

The solution methodology used here for Eqs. (25) and (26) involves a two-level updating. For stream function equation (25), the variable F is introduced such that

$$\left(1-\Delta t\frac{\partial^2}{\partial\xi^2}\right)F=\psi^n+\Delta t(\xi^2+\eta^2)\omega^n+\left(\Delta t\frac{\partial^2}{\partial\xi^2}\right)\left(\Delta t\frac{\partial^2}{\partial\eta^2}\right)\psi^n \tag{27}$$

where

$$\left(1-\Delta t\frac{\partial^2}{\partial\eta^2}\right)\psi^{n+1}=F \tag{28}$$

Similarly for vorticity equation (26), the variable G is introduced such that

$$\left[1-\Delta t\frac{\partial^2}{\partial\xi^2}+\Delta t\left(\frac{\partial\psi}{\partial\eta}\right)^n\frac{\partial}{\partial\xi}\right]G=\omega^n+\left[\Delta t\frac{\partial^2}{\partial\xi^2}-\Delta t\left(\frac{\partial\psi}{\partial\eta}\right)^n\frac{\partial}{\partial\xi}\right]\times\left[\Delta t\frac{\partial^2}{\partial\eta^2}+\Delta t\left(\frac{\partial\psi}{\partial\xi}\right)^n\frac{\partial}{\partial\eta}\right]\omega^n \tag{29}$$

where

$$\left[1-\Delta t\frac{\partial^2}{\partial\eta^2}-\Delta t\left(\frac{\partial\psi}{\partial\xi}\right)^n\frac{\partial}{\partial\eta}\right]\omega^{n+1}=G \tag{30}$$

The geometry we are dealing with is a semi-infinite body. Because the numerical calculations cover a finite domain, the buffer domain technique used by Haddad and Corke,[7] Erturk and Corke,[9] and Haddad et al.[12] was used to provide the outflow boundary condition. The approach is gradually kill the elliptic $(\partial^2/\partial\xi^2)$ terms in the governing equations in a buffer zone at the downstream end of the computational domain. To accomplish this, these elliptic terms were multiplied by a weighting factor s. At the beginning of the buffer zone, $s=1$. At the end of the buffer zone, $s=0$. In between, the s changes according to

$$s(i)=[\tanh(4)+\tanh(\arg)]/2\tanh(4) \tag{31}$$

where

$$\arg=4\{1-[2(i-i\text{buf})/(i\max-i\text{buf})]\} \tag{32}$$

On the other hand, the freestream boundary conditions are valid only at an infinitely large distance from the wall in the wall normal direction. However, the computational domain is finite. To implement the freestream boundary conditions more accurately, the stream function equation (7) is first applied at the freestream grid points with $\omega=0$. When second-order central differencing is used in both ξ and η directions, the finite difference equation resulting from Eq. (7) with $\omega=0$ requires the value of the stream function at the point outside the computational domain in the η direction. The boundary condition on the stream function at the freestream given by Eq. (15) is then central differenced at the freestream grid point. The resulting finite difference equation [from Eq. (15)] is then solved for the stream function at the point outside the computational domain. The result is then substituted back to obtain a boundary condition on the stream function at the freestream. This procedure is numerically favorable and is more accurate in that it allows the streamfunction to attain its actual value at the freestream.

V. Results and Discussion

A. Code Validation

Extensive numerical tests have been carried out to study the effect of grid size, that is, number of grid points, outflow boundary

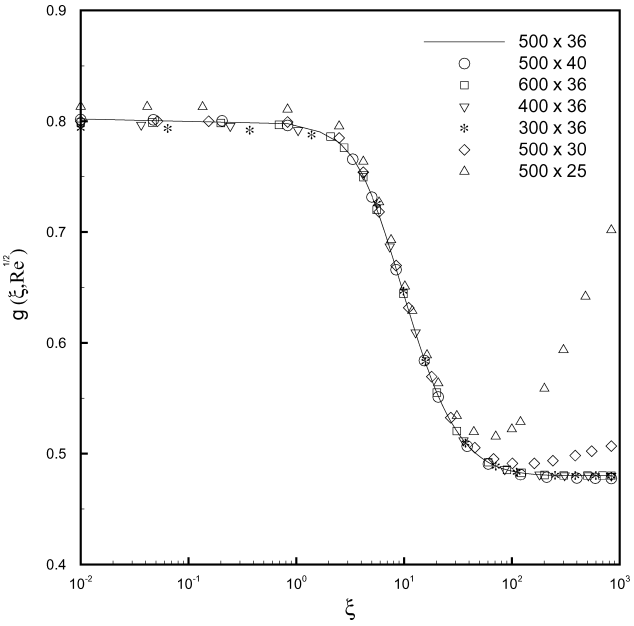

Fig. 2 Effect of computational grid size on the vorticity along the surface of the parabolic body at $Re=10$ and $\alpha=0$ deg.

location, and freestream boundary location on the numerical results. An example of the sensitivity of the numerical results to the number of computational grid points is shown in Fig. 2. This shows the wall vorticity for different computational grid sizes when $Re = 10$. The flow over the parabolic body is known to approach Blasius flow far downstream. This leads the vorticity at the wall to become invariant in the flow direction away from the leading edge. The results in Fig. 2 for grid sizes of 500×25 (triangles) and 500×30 (diamonds) show a trend far downstream that is clearly wrong. The other cases shown in Fig. 2, with a larger number of wall normal grid points, all collapse on a single curve. These show the proper downstream asymptote that agrees with a Blasius flow. The solid curve that corresponds to the grid size of 500×36 was used throughout this study.

To make a quantitative check of our numerical solutions, we compared the wall skin friction and surface pressure distributions for a family of parabolas with different nose radii to those of Haddad and Corke.[7] Note that by comparing our basic flow solutions with their solutions we indirectly also compare our results to those of Davis,[5] which agreed with those of Haddad and Corke.[7]

The skin-friction coefficient is defined as

$$C_f = \tau_w^* \big/ \rho U_\infty^2 \tag{33}$$

where $\tau_w^* = \mu(\partial u^*/\partial y^*)|_w$. If we write Eq. (33) in terms of the nondimensional stream function and use the stream function equation at the wall, we obtain

$$C_f = -\omega|_w \tag{34}$$

To compare the results, Haddad and Corke[7] followed Davis[5] and introduced the modified vorticity g into Eq. (34) so that

$$C_f = [\xi/(\xi^2 + \eta^2)]g\left(\xi, Re^{\frac{1}{2}}\right) \tag{35}$$

[Davis used the following transformation with the vorticity: $\omega = -[\xi/(\xi^2 + \eta^2)]g(\xi, \eta)$.]

Figure 3 shows the scaled skin-friction distribution over parabolic bodies with different nose radii at zero angle of attack to the mean flow. The skin friction is a maximum at the leading edge for any particular parabolic body and increases as the nose radius (Reynolds number) increases. Davis[5] pointed out that the flow over a parabolic body asymptotically approaches to Blasius flow away from the leading edge. As a check on the numerical solution, the skin-friction coefficient for a Blasius flow is shown by the dotted line. As can be seen, all of the skin-friction distributions asymptote to the Blasius value downstream of the leading edge as expected. This is also another physical check on our numerical results. The symbols correspond to the results from Haddad and Corke.[7] We note that the

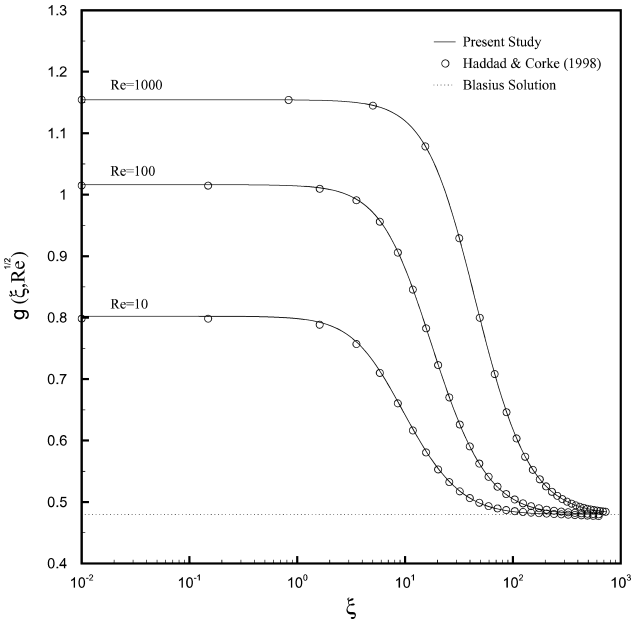

Fig. 3 Scaled skin-friction distributions on parabolic bodies with different nose Reynolds numbers at $\alpha = 0$ deg.

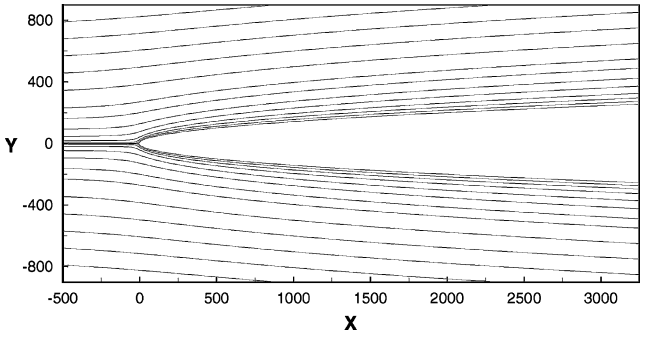

a) $\alpha = 0$ deg

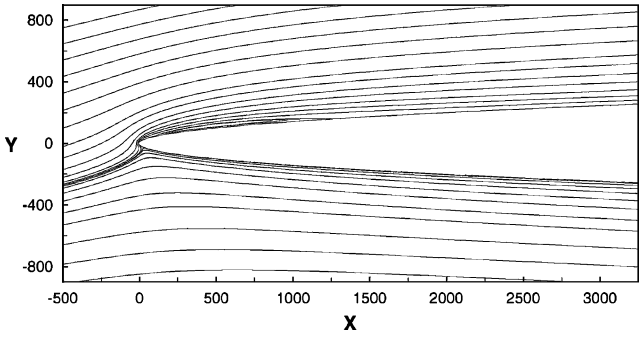

c) $\alpha = 13$ deg

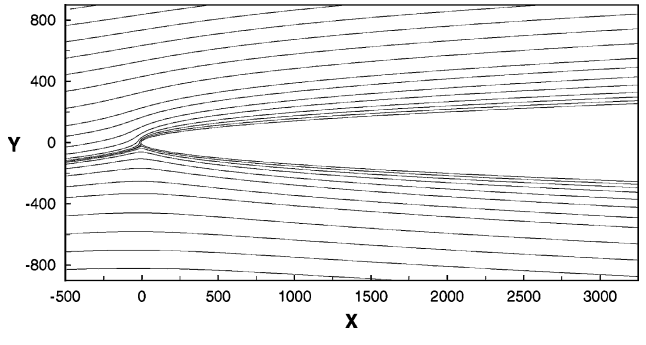

b) $\alpha = 6$ deg

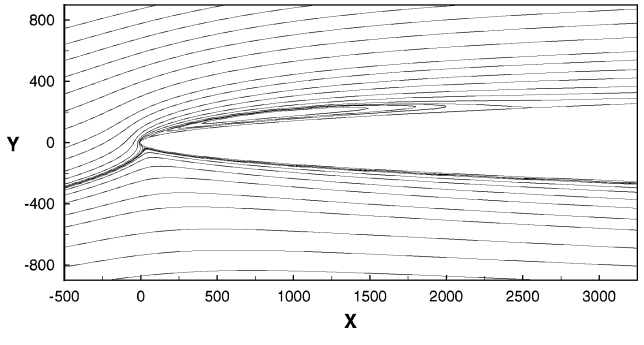

d) $\alpha = 14$ deg

Fig. 4 Velocity streamlines for flow over parabolic body at different angles of attack for $Re = 10$.

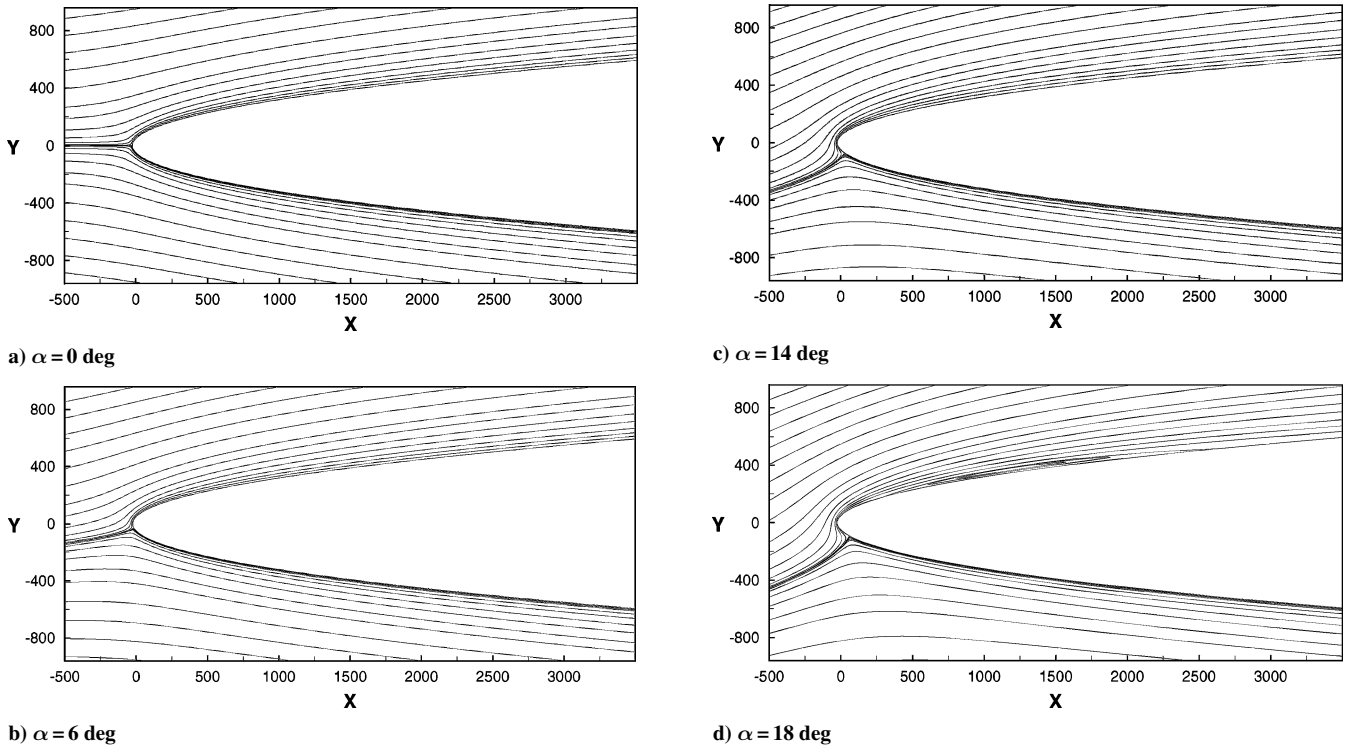

a) $\alpha = 0$ deg

c) $\alpha = 14$ deg

b) $\alpha = 6$ deg

d) $\alpha = 18$ deg

Fig. 5 Velocity streamlines for flow over parabolic body at different angles of attack for $Re = 50$.

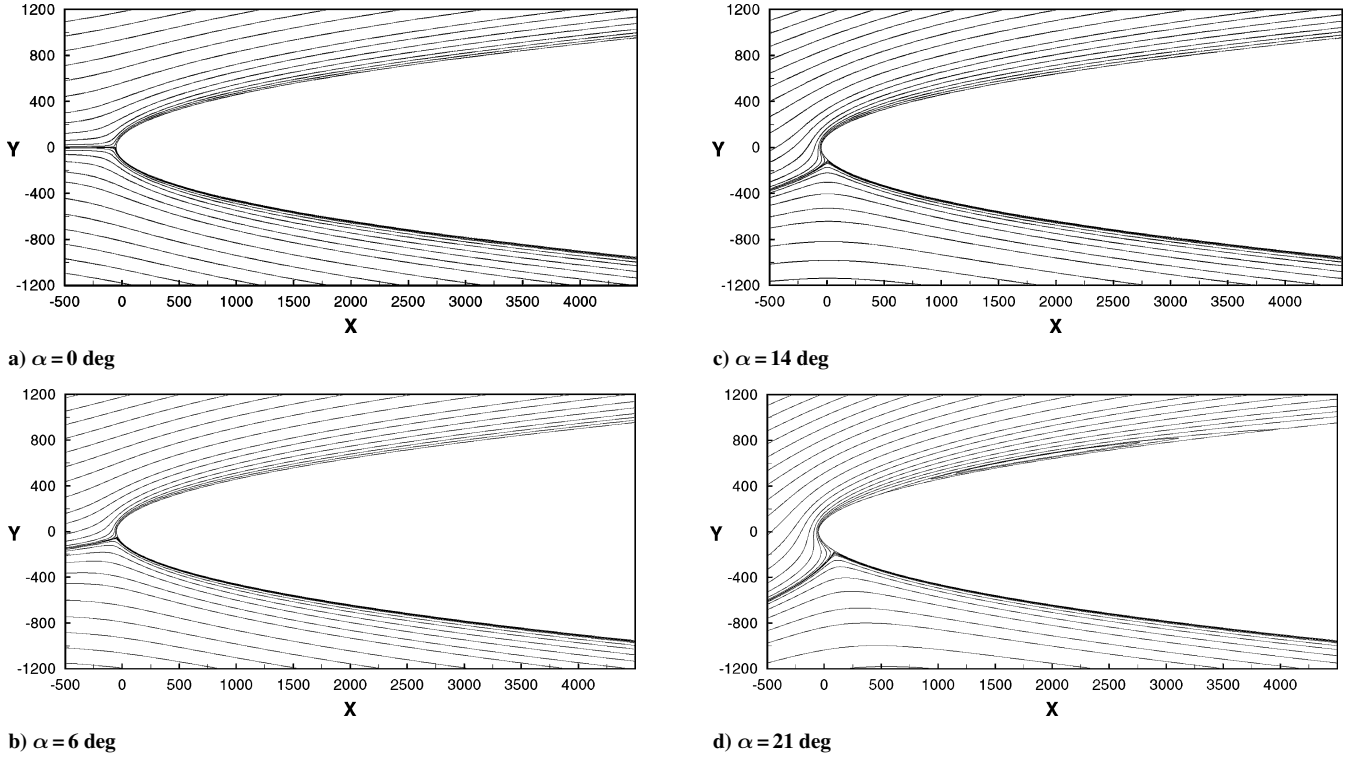

a) $\alpha = 0$ deg

c) $\alpha = 14$ deg

b) $\alpha = 6$ deg

d) $\alpha = 21$ deg

Fig. 6 Velocity streamlines for flow over parabolic body at different angles of attack for $Re = 100$.

agreement between our results and that of Haddad and Corke and also the Blasius solution is excellent.

B. Effect of Angle of Attack

The overall effect of angle of attack on the flow over the parabolic body is best shown through the velocity streamlines. These are presented for different angles of attack at $Re = 10$, 50, and 100 in Figs. 4–6. In each case, the highest angle of attack presented corresponds to one that is slightly past that where the flow separates. As expected, the angle of attack where separation occurs increases as the nose radius increases.

Figure 4 shows the velocity streamlines for the smallest nose radius corresponding to $Re = 10$. At $\alpha = 0$ deg, the stagnation streamline perfectly aligns with the body centerline axis. At the next higher angle of attack, $\alpha = 6$ deg, the stagnation streamline is curved and

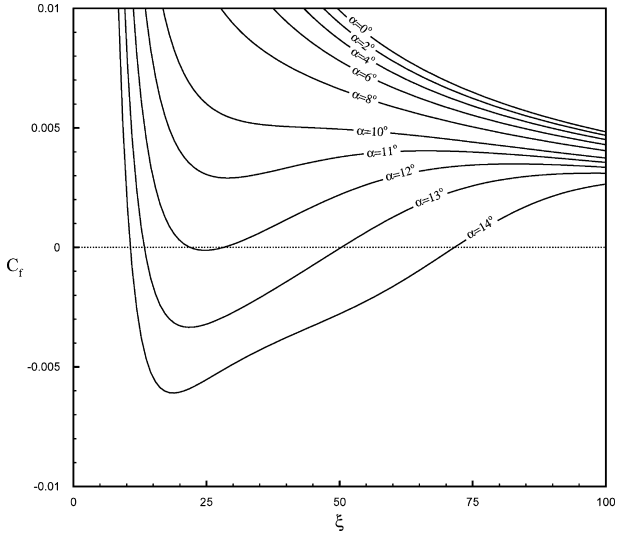

a) *Re* = 10

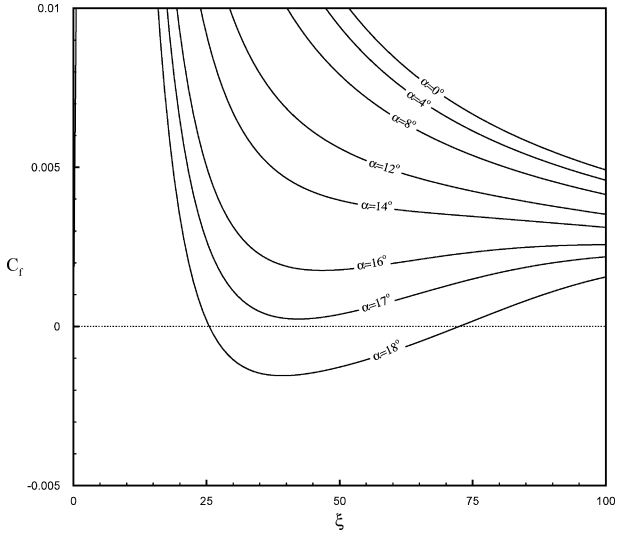

b) *Re* = 50

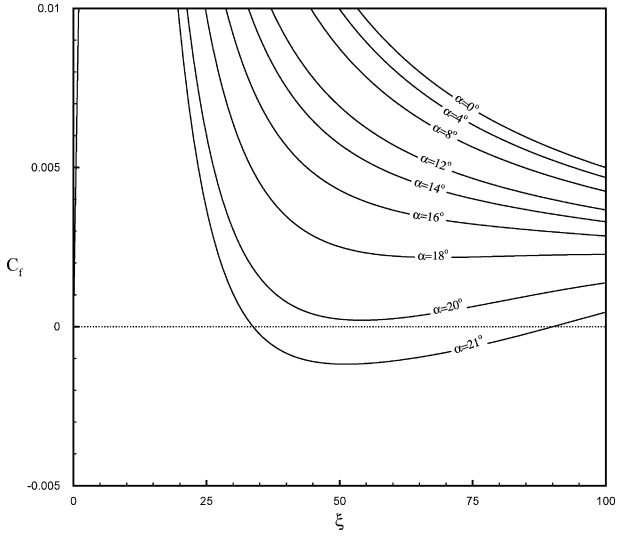

c) *Re* = 100

Fig. 7 Surface friction coefficient distributions for different angles of attack.

impacts the body below the physical leading edge. As will be shown, this results in a strong pressure gradient near the leading edge.

At $Re = 10$, the flow first separates at $\alpha = 12$ deg. The separation bubble is quite evident in the streamline pattern near the body surface at the higher angles of attack of 13 and 14 deg shown in Fig. 4. The extent of the separation bubble increases dramatically with the 1-deg increase in angle of attack.

At $Re = 50$, the flow first separates between $\alpha = 17$ and 18 deg. The streamlines shown at $\alpha = 18$ deg in Fig. 5 reveal the separation bubble. Compared to the smaller nose radius, the location of separation has moved downstream from the physical leading edge.

At the largest nose radius, $Re = 100$, the flow separates between $\alpha = 20$ and 21 deg. The streamlines shown at $\alpha = 21$ deg in Fig. 6 reveal the separation bubble in this case. The separation location again appears to have moved farther downstream from the leading edge compared to the other smaller nose radii bodies. The reasons for this will become clear from the pressure gradient distributions in these cases.

A quantitative measure of the locations of flow separation and reattachment comes from viewing the surface-friction coefficient distribution. These are shown for different angles of attack at the three nose Reynolds numbers (10, 50, 100) in Figs. 7a–7c. The value $C_f = 0$ is shown as the horizontal dotted line in Figs. 7a–7c. The upstream location where the skin friction crosses zero marks the separation location. The next downstream position where the C_f distribution crosses zero is the where the flow reattaches.

With the focus on the $Re = 10$ case shown in Fig. 7a, the flow first separates very close to $\alpha = 12$ deg. This occurs at approximately $\xi = 20$. The length of the separation bubble at this angle is fairly small, extending to approximately $\xi = 30$. As the angle of attack increases, the location of the point of flow separation moves upstream, and the length of the separation zone increases.

At $Re = 50$ (Fig. 7b), the flow first separates a little beyond $\alpha = 17$ deg. With the larger nose radius, the initial separation location has moved downstream from the leading edge. It further increases at $Re = 100$ (Fig. 7c). In this case, the flow first separates just past $\alpha = 20$ deg.

The locations of flow separation and reattachment for $Re = 10$ are summarized in Fig. 8. This demonstrates an almost linear increase in the streamwise extent of the separation zone with increasing angle of attack. In a finite length body, as the angle of attack increased, the extent of the separation zone could eventually extend past the end of the body and the flow would become fully detached. In our case with a semi-infinite body, this cannot happen, and the flow will always reattach somewhere downstream.

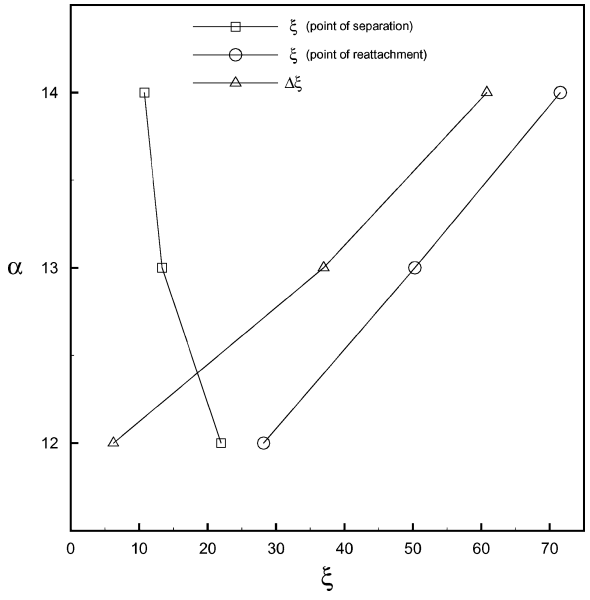

Fig. 8 Separation and reattachment locations based on surface-friction coefficients as function of angle of attack for *Re* = 10.

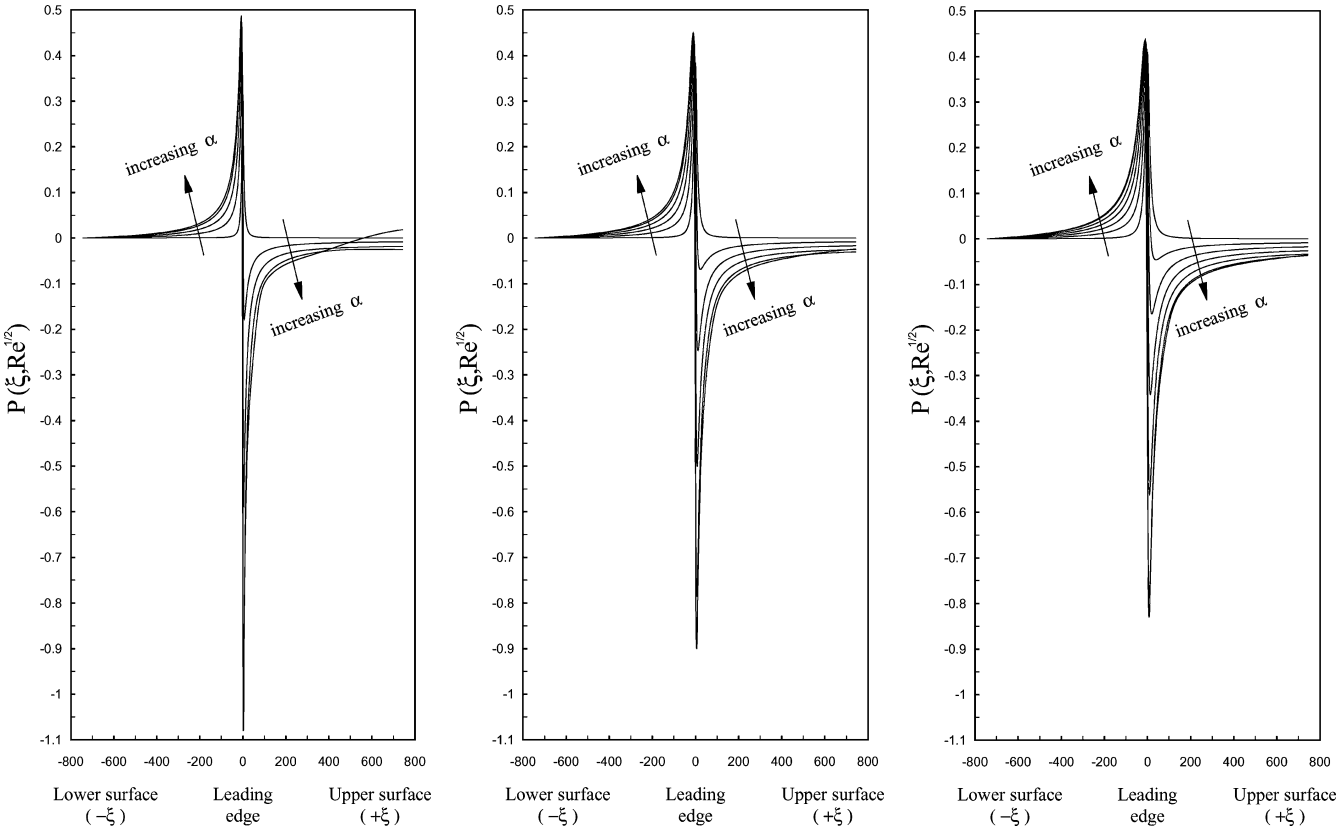

a) $Re = 10$; $\alpha = 0$, 4, 8, 12, and 14 deg **b) $Re = 50$; $\alpha = 0$, 4, 8, 12, 16, and 18 deg** **c) $Re = 100$; $\alpha = 0$, 4, 8, 12, 16, 20, and 21 deg**

Fig. 9 Surface pressure distributions over the parabolic body at different angles of attack.

To further assess the effect of angle of attack on the flow over the parabolic bodies, we consider the surface pressure distributions. To obtain an expression for the surface pressure distribution, we start with the x^*-momentum equation

$$u^*\frac{\partial u^*}{\partial x^*} + v^*\frac{\partial u^*}{\partial y^*} = -\frac{1}{\rho}\frac{\partial p^*}{\partial x^*} + \nu\left(\frac{\partial^2 u^*}{\partial x^{*2}} + \frac{\partial^2 u^*}{\partial y^{*2}}\right) \tag{36}$$

By the application of Eq. (36) at the wall (where $u^* = v^* = 0$), the introduction of the stream function ($u^* = \partial\psi^*/\partial y^*$), the nondimensionalization of the pressure [$p = (p^* - p^*_{\xi=-\infty})/(\rho U^2_\infty)$], and the use of the stream function equation, the momentum equation takes the following form in parabolic coordinates:

$$\frac{\partial p}{\partial \xi} = -\frac{\partial \omega}{\partial \eta} \tag{37}$$

Equation (37) relates the pressure gradient as a function of the vorticity variable. Haddad and Corke[7] followed Davis[5] and instead of using stream function and vorticity variables in the governing equations, they used transformed variables to remove the singularity that occurs at the leading edge in the case of an infinitely thin flat plate. To compare our results, we also used the transformed variables. Thus, following Davis,

$$P = p - [\eta/(\xi^2 + \eta^2)]g\left(0, R^{\frac{1}{2}}\right) \tag{38}$$

where g is the transformed vorticity variable and is related to vorticity as

$$g(\xi, \eta) = [-(\xi^2 + \eta^2)/\xi]\omega(\xi, \eta) \tag{39}$$

On substitution, the following is obtained:

$$\frac{\partial P}{\partial \xi} = -\frac{\partial \omega}{\partial \eta} + \frac{2\xi\eta}{(\xi^2 + \eta^2)^2}g\left(0, R^{\frac{1}{2}}\right) \tag{40}$$

We use the pressure at downstream infinity on the lower surface as a reference pressure ($P_{-\xi_{\max}} = 0$) and integrate Eq. (40) back along the surface using the trapezoidal method.

Figure 9 shows the pressure distributions for the parabolic bodies at $Re = 10$, 50, and 100 for the different angles of attack. The exact angle of attack values for each case is listed. These differ for each nose radius to encompass fully the angle where flow separation occurs. The upper surface corresponds to $\xi > 0$.

Initially at $\alpha = 0$ deg, the pressure distribution is symmetric about the leading edge. The maximum pressure occurs at the physical leading edge (stagnation point). At downstream positions, the surface pressure then decreases from the stagnation value such that the pressure gradient is always favorable.

Having the body at an angle of attack results in an asymmetric pressure distribution. In this case, the body becomes aerodynamically loaded with lower pressures on the upper surface ($\xi > 0$). The degree of asymmetry in the pressure increases with angle of attack. This is seen primarily as a narrow negative pressure that is concentrated near the leading edge. This pressure peak is associated with the acceleration of the flow around the leading edge as the stagnation point moves downstream on the lower surface, as was shown in the streamline patterns in Figs. 4–6.

We note in Fig. 9 that the magnitude of the pressure asymmetry near the leading edge increases as the nose radius decreased. That is, it is the largest for $Re = 10$ and decreases for $Re = 100$.

The factor that controls the stability of the flow to disturbances, and the ability of the flow to follow the leading-edge curvature and stay attached, is the surface pressure gradient. To highlight this, the pressure gradient $\Delta P/\Delta\xi$ is plotted in Fig. 6 for three angles of attack of the body at $Re = 10$.

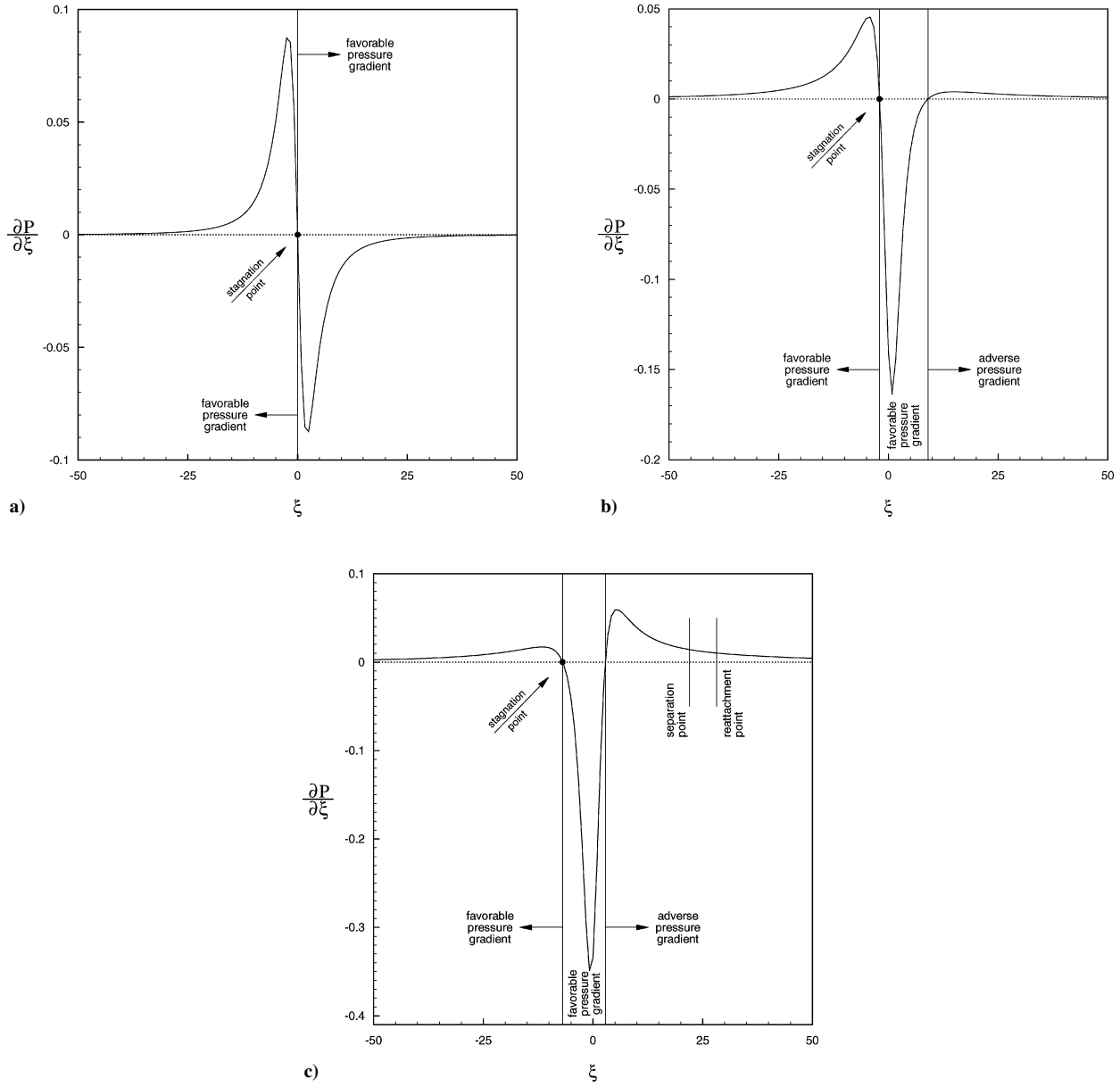

Fig. 10 For $Re = 10$, surface pressure gradient distribution over parabolic body at α = a) 0, b) 4, and c) 12 deg.

At $\alpha = 0$ deg, shown in Fig. 10a, the stagnation point is at the physical leading edge of the body, and the pressure gradient is symmetric about the centerline and everywhere favorable. In this condition, the pressure gradient asymptotes to zero relatively close to the leading edge, and the boundary layer quickly assumes a Blasius form as was shown in Fig. 3.

At a small angle of attack of 4 deg in Fig. 10b, the stagnation point moves to the pressure (lower) side of the body, and the pressure gradient is no longer symmetric. On the lower surface, the pressure gradient is favorable everywhere. Therefore, we expect the flow on the lower surface to remain attached. This is evident in the velocity streamline patterns for this angle of attack in Figs. 4–6.

On the upper (suction) surface at the 4-deg angle of attack, there is an initial favorable pressure gradient region close to the physical leading edge. This leads to an adverse pressure gradient region starting near $\xi \simeq 10$. The adverse pressure gradient at this small angle of attack is relatively small, and based on the surface shear stress at this angle in Fig. 7a, the flow is attached.

As the angle of attack is further increased, the magnitude of the adverse pressure gradient on the upper surface increases. This is evident in Fig. 10c, which corresponds to $\alpha = 12$ deg. Based on the shear stress for this condition in Fig. 7a the flow separates and reattaches at $\xi \simeq 20$ and 30, respectively. These locations are indicated in Fig. 10c. Note that the flow separation does not occur at the point of the largest adverse pressure gradient. Therefore, the pressure gradient sign or magnitude is not a sufficient criteria to predict if or where flow separation occurs. Rather, the shape of the mean velocity profile needs to also be considered. This will be done next by looking at the shape factor.

We present some of the mean velocity profiles in the region between the leading edge and the point of separation for $Re = 10$ and $\alpha = 12$ deg in Fig. 11. Figure 11a shows the profiles for the full extent from the body surface to freestream. Figure 11b is magnified views closest to the body surface. The profile at $\xi = 0$ corresponds to the physical leading edge. As was shown for this case in Figs. 4–6, the stagnation point at this angle of attack is on the pressure side of the body. Therefore, the flow is accelerating around the leading edge. The mean velocity profiles reflect this through a noticeable overshoot near the body surface.

At $\xi = 5$, the pressure gradient just becomes adverse. The velocity profile near the wall a this location has not yet responded to

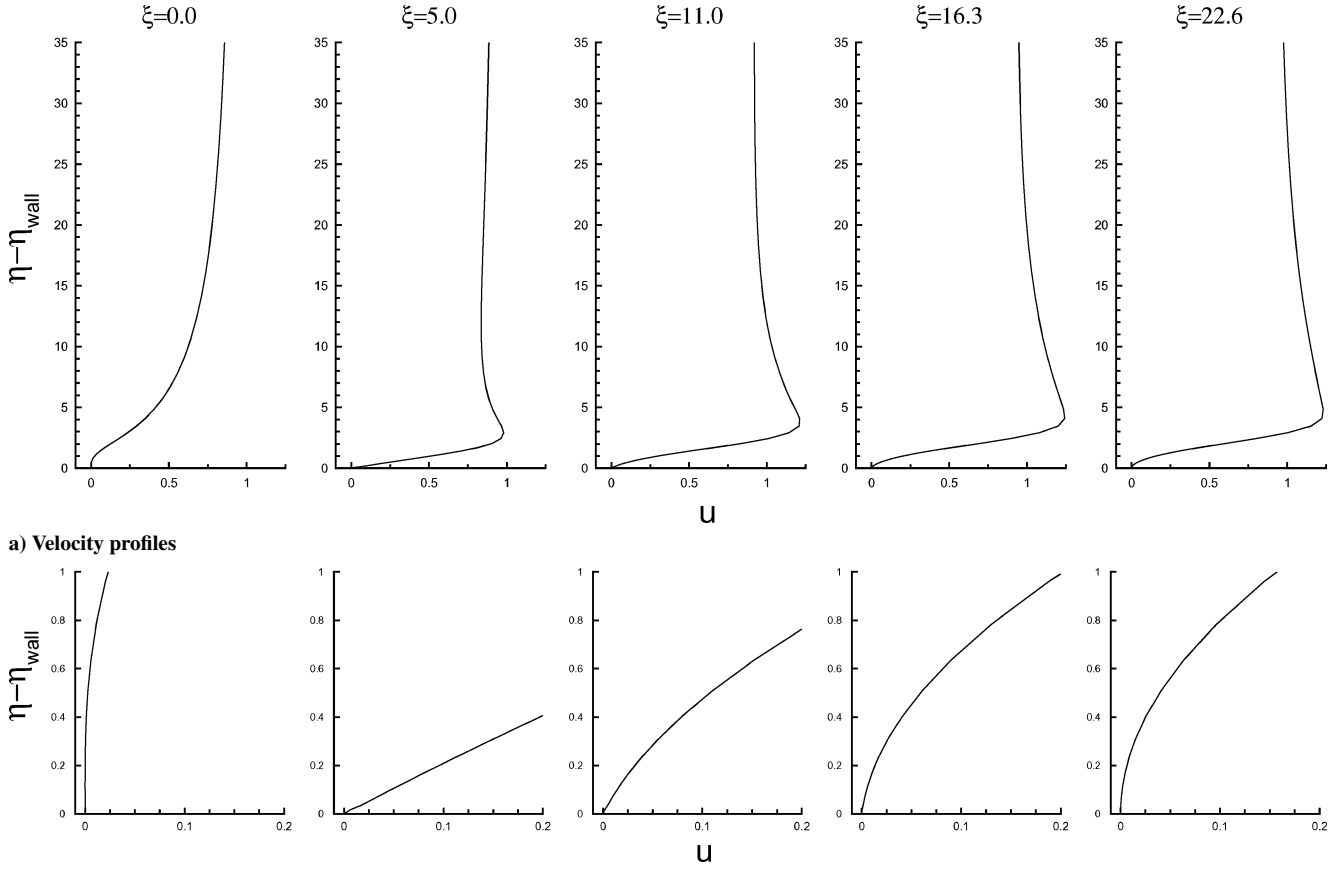

Fig. 11 Velocity profiles at different streamwise locations from stagnation to the point of separation for $\alpha = 12$ deg at $Re = 10$.

the changing gradient and has a stable linear distribution near the wall.

As the adverse pressure gradient grows in magnitude along the surface, the mean velocity profiles develop an inflexional shape. This is most evident in the magnified views near the wall. The inflexion grows with downstream distance until the mean velocity gradient $(\mathrm{d}u/\mathrm{d}\eta)$ at the wall is zero ($C_f = 0$) and the flow separates. This occurs at $\xi = 22.6$, which is the most downstream profile shown in Fig. 11.

A global (integrated) quantity that reflects the tendency of the boundary layer to separate is the shape factor $H = \delta_1/\delta_2$, where δ_1 and δ_2 are the boundary-layer displacement and momentum thicknesses, respectively. The shape factor distributions for the three nose Reynolds numbers (10, 50, and 100) at selected angles of attack are shown in Fig. 12. For $Re = 10$, the shape factor at $\alpha = 0$ and at a postseparation (12 deg) are presented. For $Re = 50$ and 100, the shape factor distribution is shown for postseparation angles of 18 and 21 deg, respectively.

The shape factor distribution at $\alpha = 0$ deg for $Re = 10$ is representative of the other Reynolds number cases without angle of attack. For this, the distribution is symmetric about the $\xi = 0$ centerline of the body. The dotted line represents $H = 2.59$, which is the theoretical value for a Blasius boundary layer (see Ref. 16). Downstream, away from the leading edge, the shape factors in our cases approach this value. We expect that our results would match this for an infinitely thin ($R = 0$) body (without a leading edge). With finite thickness, the value asymptotes to a slightly lower value.

The large changes in the shape factor occur relatively close to the leading edge, where the large pressure gradients are occurring. At angles of attack, the shape factor distribution is no longer symmetric about the body centerline. In general, on the suction (upper) side of the body, the shape factor peaks above the 2.59 Blasius value in the region of the adverse pressure gradient. On the pressure (lower) side of the body, the opposite is true. There, the shape factor peaks below the Blasius value in the region of the strong favorable pressure gradient.

Table 1 Shape factors at separation and reattachment for different cases

Re	α, deg	H_s	H_r
10	12	4.59	4.48
50	18	4.51	4.30
100	21	4.59	4.27

We seek to correlate values of the shape factor with the locations of flow separation and reattachment for the flow over the parabolic body. Approximate methods for two-dimensional laminar flows[16] have provided a criterion for separation of $H = 3.5$. This criterion is based on a special family of profile shapes attributed to Pohlhausen that assume a fourth degree polynomial for the velocity as a function of the dimensionless distance from the wall. Our velocity profile shapes, such as shown in Fig. 11, do not fit into the Pohlhausen family. In particular, because of the strong acceleration of the flow near the leading edge, there exists, in our case, a strong overshoot in the velocity near the wall even at separation. However, the approximate method suggests that there might be a consistency in the shape factor values for our different cases that can be correlated with the separation location.

When we examine the shape factors at the separation and reattachment locations for the cases listed in Table 1, we indeed observe a fairly consistent result that $H \simeq 4.5$. This includes the three nose radius Reynolds numbers at postseparation angles of attack. Thus, the shape factor H seems to track the evolution of the bulk boundary layer fairly well, and in this special case of a parabolic leading edge, H can be used to provide a criterion for separation.

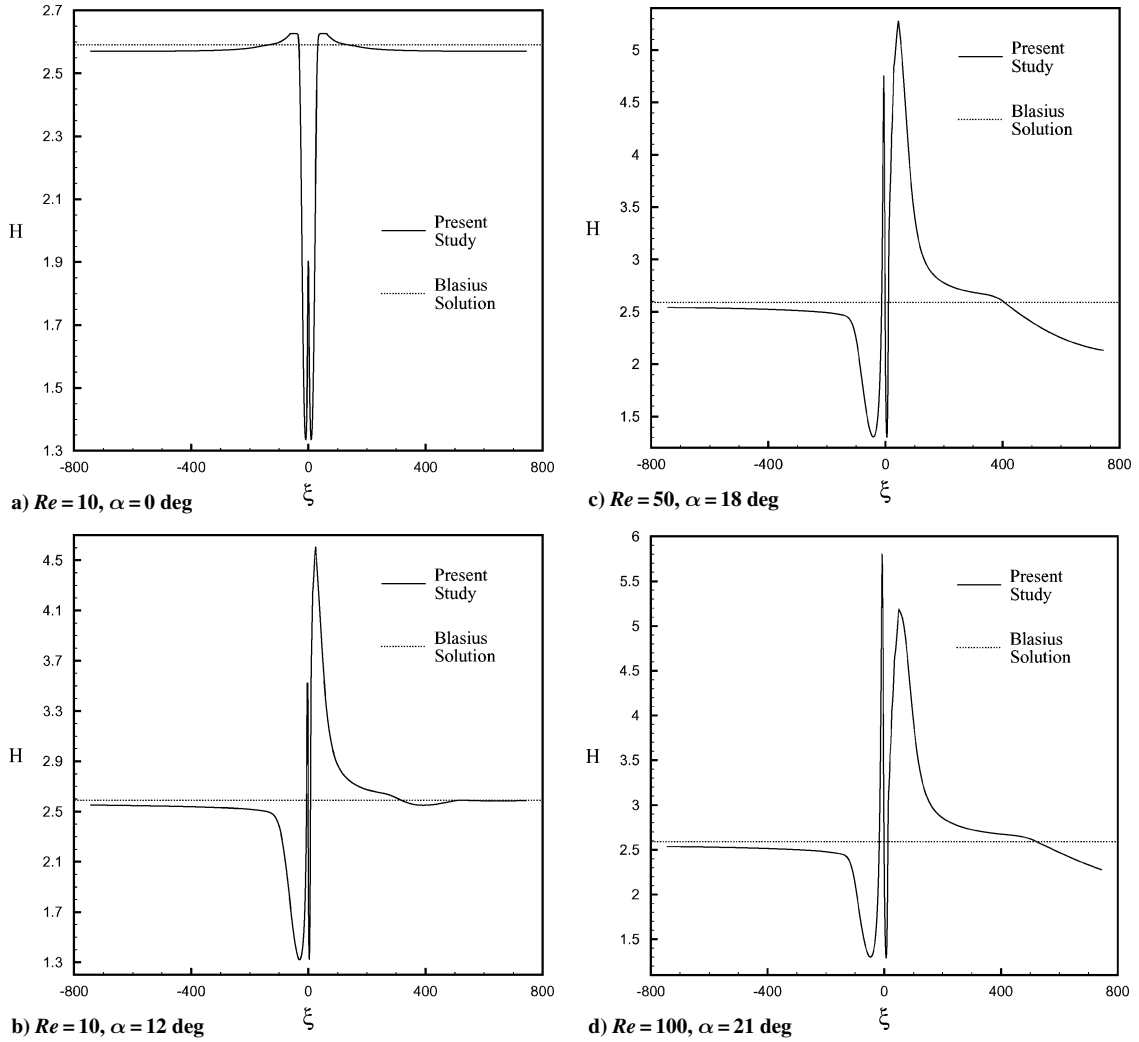

Fig. 12 Shape factor distributions for $\alpha = 0$ deg at $Re = 10$ and postseparation angles of attack for $Re = 10$, 50, and 100.

VI. Conclusions

The steady, two-dimensional incompressible N–S equations in stream function and vorticity form in parabolic coordinates were solved numerically to study the flow past semi-infinite parabolic bodies at angles of attack. The importance of the flow over parabolic bodies comes from the fact that aerodynamic shapes designed for subsonic flow generally have finite thickness distributions with a parabolic leading edge.

The results at zero angle of attack compared very well with those of Davis[5] and Haddad and Corke.[7] In addition, far from the leading edge, an expected correspondence to Blasius flow was found. In this case, a favorable pressure gradient existed everywhere over the body.

At positive angles of attack, the body became aerodynamically loaded with lower pressures on its upper surface. In this case, the stagnation point moved to the lower surface of the body, which then led to a surface pressure distribution that was initially favorable but then became adverse. The magnitude of the adverse pressure gradient increased with increasing angle of attack. At large enough angles of attack, the flow separated in the adverse pressure gradient region.

The angle of attack where separation first occurred increased with increasing nose radius Reynolds number. At $Re = 10$, $\alpha_s = 12$ deg. At the largest Reynolds number studied, $Re = 100$, $\alpha_s \simeq 21$ deg.

In all of the cases examined, the flow separation was followed by a reattachment that defined a separation zone. For a given nose radius, we observed an almost linear increase in the streamwise extent of the separation zone with increasing angle of attack. The length of the separation zone also increased as the nose radius Reynolds number increased.

A shape factor, $H = \delta_1/\delta_2$, of approximately 4.5 was consistently found to occur at the separation and reattachment locations. This included all of the examined nose radius Reynolds numbers at postseparation angles of attack. Thus, in this special case of a parabolic leading edge, it might be used to provide a criterion for separation.

The parabolic shape at angles of attack appears to be ideal for studying the impact of flow separations on the acoustic receptivity of boundary-layer instabilities. The special characteristics are that a closed separation bubble forms close to the leading edge, which is well upstream of the minimum critical branch 1 value of the T–S neutral curve. Following the separation bubble, the boundary layer quickly approaches a Blasius distribution so that the linear stability characteristics are similar to those before separation. For the largest angle of attack examined, the distance between the leading edge and separation location, and the length of the separation bubble, are small fractions of the T–S wave length, even at the highest amplified frequencies. For the dimensionless frequency of $2\pi f\nu/U_\infty^2 = 230 \times 10^{-6}$ used by Haddad and Corke,[7] the T–S wavelength is approximately four times the distance from the leading edge to the end of the separation bubble. At more amplified frequencies that are more likely to lead to transition, for example, 120×10^{-6}, the difference will be even larger. Both the leading edge and separation bubble should act as acoustic receptivity sites, where the long wavelength sound can be converted into the shorter wavelength vortical fluctuations that are appropriate to the T–S instability. However, being a fraction of a wavelength apart, we do not expect them to compete or exhibit the type of frequency selection mechanism that was found to exist in the branch 1 receptivity coefficient of an elliptic leading edge attached to a flat plate, observed

by Saric and White[11] and simulated by Wanderley and Corke,[10] in which the distance from the leading edge to junction was multiple T–S wavelengths. Therefore, this geometry should be excellent in documenting the single impact of flow separations on boundary-layer transition and contrasting its effect to that of the leading edge alone.

Acknowledgments

E. Erturk is grateful for the financial support of the Gebze Institute of Technology. O. Haddad is grateful for the financial support provided by the University of Notre Dame Center for Flow Physics and Control. O. Haddad is also grateful for Jordan University of Science and Technology for granting sabbatical leave to participate in this work.

References

[1]Hammerton, P. W., and Kerschen, E. J., "Boundary-Layer Receptivity for a Parabolic Leading Edge. Part 2, The Small Strouhal Number Limit," *Journal of Fluid Mechanics*, Vol. 353, 1997, pp. 205–220.

[2]Van Dyke, M. D., "Higher Approximations in Boundary-Layer Theory Part 1. General Analysis," *Journal of Fluid Mechanics*, Vol. 14, 1962, pp. 161–177.

[3]Davis, R. T., "Laminar Incompressible Flow past a Semi-Infinite Flat Plate," *Journal of Fluid Mechanics*, Vol. 27, 1967, pp. 691–704.

[4]Dennis, S. C. R., and Walsh, J. D., "Numerical Solutions of Steady Symmetric Viscous Flow past a Parabolic Cylinder in a Uniform Stream," *Journal of Fluid Mechanics*, Vol. 50, 1971, pp. 801–814.

[5]Davis, R. T., "Numerical Solution of the Navier–Stokes Equations for Symmetric Laminar Incompressible Flow past a Parabola," *Journal of Fluid Mechanics*, Vol. 51, 1972, pp. 417–433.

[6]Gatski, T. B., "Mean Flow Validation for Numerical Study of Leading Edge Boundary Layer Receptivity," *Applied Mechanics Reviews*, Vol. 43, No. 5, 1990, pp. 181–184.

[7]Haddad, O. M., and Corke, T. C., 1998, "Boundary Layer Receptivity to Free-Stream Sound on Parabolic Bodies," *Journal of Fluid Mechanics*, Vol. 368, 1998, pp. 1–26.

[8]Erturk, E., "Leading Edge Boundary Layer Receptivity to Oblique Free Stream Acoustic Waves on Parabolic Bodies," Ph.D. Dissertation, Dept. of Mechanical and Aerospace Engineering, Illinois Inst. of Technology, Chicago, May 1999.

[9]Erturk, E., and Corke, T. C., "Boundary Layer Leading-Edge Receptivity to Sound at Incidence Angles," *Journal of Fluid Mechanics*, Vol. 444, 2001, pp. 383–407.

[10]Wanderley, J. B., and Corke, T. C., "Boundary Layer Receptivity to Free-Stream Sound on Elliptic Leading Edges of Flat Plates," *Journal of Fluid Mechanics*, Vol. 429, 2001, pp. 1–21.

[11]Saric, W. S., and White, E. B., "Influence of High-Amplitude Noise on Boundary-Layer Transition to Turbulence," AIAA Paper 98-2645, Jan. 1998.

[12]Haddad, O. M., Abu-Qudais, M., and Maqableh, A. M., "Numerical Solutions of the Navier–Stokes and Energy Equations for Laminar Incompressible Flow past Parabolic Bodies," *International Journal of Numerical Methods for Heat and Fluid Flow*, Vol. 10, No. 1, 2000, pp. 80–93.

[13]Haddad, O. M., Al-Nimr, M., and Abu-Ayyad, M., "Numerical Simulation of Forced Convection Flow past a Parabolic Cylinder Embedded in Porous Media," *International Journal of Numerical Methods for Heat and Fluid Flow*, Vol. 12, No. 1, 2002, pp. 6–28.

[14]Anderson, D. A., Tannehill, J. C., and Pletcher, R. H., *Computational Fluid Mechanics and Heat Transfer*, McGraw–Hill, New York, 1984, Chap. 5.

[15]Erturk, E., "Numerical Solutions of 2-D Steady Incompressible Driven Cavity Flow at High Reynolds Numbers," *International Journal for Numerical Methods in Fluids* (submitted for publication).

[16]Schlichting, H., *Boundary Layer Theory*, McGraw–Hill, New York, 1968, Chap. 10.

H. Reed
Associate Editor